VIP *Very Important Paper*

Special Issue

Cobalt Nanoparticles Confined in Carbon Cages Derived from Zeolitic Imidazolate Frameworks as Efficient Oxygen Electrocatalysts for Zinc-Air Batteries

Xuncai Chen,[a] Zixun Yu,[a] Li Wei,[a] Ziwen Yuan,[a] Xiao Sui,[a] Yanqing Wang,[b] Qianwei Huang,[c] Xiaozhou Liao,[c] and Yuan Chen*[a]

Rechargeable zinc (Zn)-air batteries are a potential solution to effectively incorporate electricity generated from renewable energy sources into our daily consumption, which requires electrocatalysts to catalyze the oxygen-reduction reaction (ORR) and the oxygen evolution reaction (OER) on the air electrode. Here, we report a high-performance bifunctional oxygen electrocatalyst by confining cobalt (Co) nanoparticles in nitrogen (N)-doped porous carbon cages derived from a metal-organic framework, i.e., ZIF-8. Co precursors were first impregnated into ZIF-8 by a double solvent method. Afterward, carbonization produces highly dispersed Co nanoparticles (with the average diameter of 6.2 nm) confined in N (11.4 at.%) doped porous carbon cages (434.5 $m^2 g^{-1}$). This electrocatalyst exhibits excellent catalytic activity for both ORR and OER with long-term stability. It delivers a half-wave potential of 0.838 V vs. reversible hydrogen electrode, an electron transfer number of 3.9 for ORR, an overpotential of 0.411 V at 10 mA cm^{-2}, and a Tafel slope of 71.2 mV dec^{-1} for OER. Rechargeable Zn-air batteries assembled using this electrocatalyst demonstrate an open-circuit potential of 1.48 V, a specific capacity of 731.1 mAh g^{-1}, and good rechargeability. The simple and efficient method can confine metal nanoparticles in porous carbon cages, which can be further explored to synthesize novel electrocatalysts for various energy conversion applications.

1. Introduction

The current overdependence on fossil fuels as energy sources has raised significant environmental concerns.[1] A potential solution is to generate electricity from renewable energy sources (e.g., solar, wind and tide) and incorporate it into our daily consumption through efficient electrochemical energy devices, such as fuel cells, supercapacitors, and batteries.[2–3] Among various electrochemical energy devices, there is considerable recent attention on electrically rechargeable zinc (Zn)-air batteries due to their high theoretical energy density, environmental-friendliness, affordability, and safety.[4–13] Zn-air batteries operate on the reversible electrochemical reaction: 2Zn + O$_2$↔2ZnO (E = 1.65 V vs. standard hydrogen electrode (SHE)) between a Zn metal electrode and an air electrode. The oxygen reduction reaction (ORR) and oxygen evolution reaction (OER)

taking place on air electrodes during the battery discharging and charging is critical for the battery performance.[14–16] Poor catalytic performances in O$_2$ electrocatalysts are impeding the applications of rechargeable Zn-air batteries.[17–18] Other than catalysts based on precious metals and their oxides,[19–21] several types of recently studied bifunctional O$_2$ electrocatalysts for rechargeable Zn-air batteries include metal-nitrogen-carbon (metals refer to transition metals, such as Fe, Co, Ni),[22–23] perovskites,[24–25] transition metal oxides,[26–29] and heteroatom-doped carbons.[30–32]

Catalysts based on metal or metal oxide nanoparticles often suffer from nanoparticle dissolution, sintering, and agglomeration in reaction conditions.[33] To overcome these obstacle, various catalyst substrates, such as carbon materials (e.g., active carbon, porous carbon, carbon nanotubes, or graphene), metal carbides, mesoporous silica, and conducting polymers, have been developed to stabilize these nanoparticles.[33] Among them, porous carbon materials offer large surface to host nanoparticles, abundant pores to enable efficient mass transport, and relatively low cost, and have been used in a variety of catalysts.[7,34–36] In particular, their porous structure can embed, disperse, and protect catalytically-active nanoparticles from leaching and aggregation. Besides, heteroatom dopants, such as N or S, can be introduced into graphitic carbon frameworks to create synergistic effects between nanoparticles and carbon substrates, resulting in improved catalyst performance.[37–44]

The synthesis of nanoparticles encapsulated by porous carbon cages usually relies on either hard or soft template methods. Hard templates, such as silica nanoparticles, have been used to precisely control the pore structures of carbon cages. However, corrosive acids (e.g., HF) or bases (e.g., NaOH)

[a] X. Chen, Z. Yu, Dr. L. Wei, Z. Yuan, X. Sui, Prof. Dr. Y. Chen
School of Chemical and Biomolecular Engineering
The University of Sydney
Sydney, New South Wales 2006, Australia
E-mail: yuan.chen@sydney.edu.au

[b] Dr. Y. Wang
The University of Tokyo
Faculty of Engineering
Yayoi, Bunkyo-ku, Tokyo 113-0032, Japan

[c] Q. Huang, Prof. Dr. X. Liao
The University of Sydney
School of Aerospace
Mechanical & Mechatronic Engineering
Sydney, New South Wales 2006, Australia

are often required to remove hard templates.[7,35–36] Alternatively, soft templates, such as surfactants and organic polymers, can effectively incorporate nanoparticles, and they can be easily removed by high-temperature carbonization, resulting in porous carbon materials. However, the soft template approach often creates an uneven distribution of nanoparticles in porous carbon substrates.[45] Carbon materials derived from metal-organic frameworks (MOFs) have emerged as a new class of promising porous carbon substrates, which can provide confined pore spaces to limit the nucleation of metal nanoparticles.[46–47]

There are two main approaches to incorporate metal species in MOFs. One is to substitute metal ions in MOFs during their synthesis directly. For example, carbonization of a Co-substituted zeolitic imidazolate framework (ZIF-67) yields Co nanoparticles on carbon substrates.[48] The other is to deposit additional metal precursors on synthesized MOF surfaces, such as Zn-based ZIF-8. The second approach shows some advantages over the first approach in controlling the size of metal nanoparticles better and creating stronger synergistic effects between metal nanoparticles and carbon substrates.[49–51] Several methods have been used to deposit metal precursors into MOFs, including chemical vapor deposition,[52] solid grinding,[53] and solution infiltration.[54–55] Many metal nanoparticles can be loaded on MOFs via the solvent-free chemical vapor deposition or solid grinding methods. However, expensive volatile metal precursors are often required by these methods. Further, it is not easy to precisely control where metal precursors would deposit on MOFs.[56] Similarly, although it is simple to load metal precursors in MOFs by the regular solution infiltration method, it is challenging to precisely control whether the metal precursors stay inside or outside of MOFs. Some precursors are inevitably deposited on external surfaces of MOFs, which would aggregate into large metal/metal oxide particles during reduction conditions. Recently, a double-solvent impregnation method was developed to introduce metal precursors into MOFs controllably.[57] Because some MOFs have large cages with hydrophilic internal environments, an exact quantity (no more than the pore volume of MOFs) of metal precursor aqueous solutions is first dispersed in a large volume of low-boiling-point organic solvent. Then, when MOFs are exposed to the mixture, most of the aqueous solutions can be incorporated inside MOF pores through capillary forces and hydrophilic interactions. The method has shown significant advantages in controlling the incorporation of metal precursors into MOFs for some applications.[56]

Herein we present a facile method to confine well-dispersed Co nanoparticles in nitrogen-doped porous carbon cages. A commercial metal-organic framework (ZIF-8) was used as a sacrificial template. Co precursors were incorporated into ZIF-8 by the double-solvent impregnation method, followed by high-temperature carbonization to convert ZIF-8 into porous carbon cages. Characterization of the resulting materials shows that highly dispersed Co nanoparticles are confined in porous carbon cages with crystalline carbon shells. The materials exhibit superior catalytic activities for both ORR and OER. We further explored their applications as oxygen electrocatalysts

for rechargeable Zn-air batteries, demonstrating excellent energy storage performance.

Experimental Section

Chemicals

ZIF-8 (Basolite® Z1200, Sigma-Aldrich) has the pore volume 0.53 cm^3/g. Cobalt (II) chloride hexahydrate (Sigma-Aldrich, ACS reagent, 98%), anhydrous n-hexane (Sigma-Aldrich) and ethanol (C_2H_5OH, 99%) were used as received.

Synthesis of Electrocatalysts

Co nanoparticles confined in N-doped porous carbon cages (denoted as Co/N-PCC) were prepared by the modified double solvent method.[46] Typically, 0.2 g of commercial ZIF-8 was first dried in a vacuum oven at 30 °C overnight and then dispersed in 40 mL hydrophobic solvent (n-hexane) by bath sonication for 15 min. Afterward, 0.106 mL of hydrophilic solvent (aqueous solution containing 20.3 mg of $CoCl_2 \cdot 6H_2O$) was added to the hydrophobic solution dropwise in 30 min under vigorous stirring. The mixture was further shaken for 12 hours on an orbital shaker. The resultant light pink-colored solid powders were collected by filtration, washed using methanol for several times, and then dried in ambient air. Next, the dried solid powders were calcined under in a flowing Ar environment (100 sccm, 99.99%, Coregas) in a tube furnace, the temperature was increased to 900 °C at a heating rate of 5 °C min^{-1} and kept at that temperature for 2 hours, resulting in the black-colored powder electrocatalysts (Co/N-PCC). For comparison, a reference catalyst was prepared under a similar synthesis condition except that $CoCl_2 \cdot 6H_2O$ was not added in the aqueous solution. The resulting carbon electrocatalyst was denoted as N-PCC (N-doped porous carbon cage). Aqueous solutions were prepared using deionized water ($\geq$ 18 MΩ).

Characterization of Physicochemical Properties

The morphology and structure of the electrocatalysts were examined by scanning electron microscope (SEM, Ultra-Plus, Zeiss) and transmission electron microscope (TEM, JEM-2100F, JEOL). Elemental mappings of the electrocatalyst surfaces were acquired by energy-dispersive X-ray spectroscopy (EDX) on the SEM. Their specific surface area and porosity were characterized using a surface area analyzer (Autosorb-1, Quantachrome Instruments). Nitrogen adsorption and desorption isotherms were recorded at 77 K. Their specific surface areas were calculated using the Brunauer-Emmett-Teller (BET) method. Their elemental compositions were analyzed by both EDX and inductively coupled plasma atomic emission spectroscopy (ICP-AES, Varian, Agilent). Raman spectra of the electrocatalysts were collected on a Raman microscope (inVia, Renishaw) under a 532 nm laser. The crystallinity of the electrocatalysts was examined by both X-ray powder diffraction (XRD) using an XRD diffractometer (XRD-6000, Shimadzu) and TEM. Their surface elemental compositions were further examined by X-ray photoelectron spectroscopy (XPS, AXIS 165, Kratos).

Preparation of Electrodes

Electrocatalyst ink was prepared by dispersing 5 mg of the electrocatalysts in 1 mL of water/isopropanol solution (1:9 v/v) with 0.5 wt.% Nafion 117 (Sigma-Aldrich) in an ultrasonic bath. For OER and ORR activity tests, working electrodes were prepared by drop

casting 10 μL of the electrocatalyst ink on a pre-polished glassy carbon rotating disk electrodes (RDE) with the surface area of 0.196 cm^2 (Pine Instrument). The electrodes were dried in the vacuum oven overnight and yielded the catalyst mass loading of ~0.25 mg cm^{-2}. Commercial electrocatalysts, IrO$_2$ (99.9%, Sigma-Aldrich) and Pt/C (20 wt% Pt on Vulcan XC-72 carbon black), were used to prepare reference electrodes with the same mass loading. At least three electrodes were prepared using the individual catalyst to ensure the reproducibility of the experimental results.

Testing of Electrocatalytic Performances

All electrocatalytic activity tests were performed using an electrochemical workstation (CHI660E, CHI Instrument) using the three-electrode configuration. RDEs loaded with electrocatalysts served as working electrodes, a carbon rod (99.999%, Strem Chemicals) was used as the counter electrode, and a saturated calomel electrode (SCE) worked as the reference electrode. All potentials were calibrated to a reversible hydrogen electrode (RHE). The ORR activity tests were conducted in 0.1 M KOH electrolyte, which was first purged by Ar (Coregas, 99.99%) for 30 min and then O$_2$ for another 30 min. CV curves before and after O$_2$ saturation were recorded at the scan rate of 100 mV s^{-1}. The electron transfer number (n) was calculated by the Koutechky-Levich (K–L) equation (see Supporting Information (SI) for details). OER activity was measured in O$_2$ (Coregas, 99.999%) saturated 0.1 M KOH electrolyte. The OER polarization linear sweep voltammetry (LSV) scan curves were collected at the scan rate of 5 mV s^{-1} with 95% iR-compensation. The Tafel plots were collected at the scan rate of 2 mV s^{-1}. During the OER stability test, O$_2$ gas product was collected every 30 min and analyzed using a gas chromatography (GC) (Agilent, 6890 N).

Assembly and Testing of Zn-Air Batteries

Zn plates (1×1 cm^2) (Goodfellow, 99.9%) were used as Zn metal electrodes. Air electrodes were prepared by dipping ~0.4 mL of 5 mg mL^{-1} electrocatalyst ink (as bifunctional air electrocatalysts) on both sides of pressed carbon cloth (1×1 cm^2), resulting in the specific mass loading of 1 mg/cm^2 on the electrode surface. For comparison, the mixture of commercial Pt/C (Sigma Aldrich, 20% Pt on Vulcan XC72) and IrO$_2$ (Sigma Aldrich) electrocatalysts (at 1 to

1 mass ratio with the total specific catalyst mass loading of 1 mg/cm^2) were used to prepare reference air electrodes. The air electrodes served as both the gas diffusion layer and the current collector in the assembled Zn-air batteries. The void between two electrodes was filled with an electrolyte containing 6 M KOH and 0.2 M ZnCl$_2$. The performance of assembled Zn-air batteries was tested on a battery testing station (CT2001, Land) in the ambient air condition.

2. Results and Discussion:

2.1. Synthesis of the Co/N-PCC Electrocatalyst

As illustrated in Figure 1, a two-step synthesis method was used to synthesize the Co/N-PCC electrocatalyst. In the first step, Co ions were immobilized inside the pores of ZIF-8 by the double-solvent method.[58] ZIF-8 was chosen because of its good stability in aqueous solution, large specific surface area (up to 1800 m^2/g), and accessible hydrophilic cavities (about 1.2 nm in diameter with pore apertures of 0.34 nm).[59–60] The double-solvent method employed both a hydrophilic solvent (water) and a hydrophobic solvent (hexane). The aqueous solution can be adsorbed within the hydrophilic cavities, while a large amount of hexane solvent can efficiently disperse ZIF-8 particles. The volume of the aqueous solution of Co precursors was set equal to the pore volume of the adsorbent (ZIF-8) at 0.53 cm^3/g.[61] For 0.2 g of ZIF-8 particles used in each synthesis batch, 0.13 mL aqueous solution of CoCl$_2$·6H$_2$O was used. Because ZIF-8 has a large specific surface area, the small amount of aqueous solution used can efficiently enter the hydrophilic pores due to capillary forces, and the large pore apertures also allow Co^{2+} ions to enter, which minimizes the deposition of Co^{2+} on the outer surface. After the immobilization, the color of ZiF-8 changed from white to pale green (see Figure S1 in SI). It should be noted that the double-solvent method has been previously used to immobilize Pt nanoparticles in MIL-101 for liquid and gas phase reactions.[46,58] To
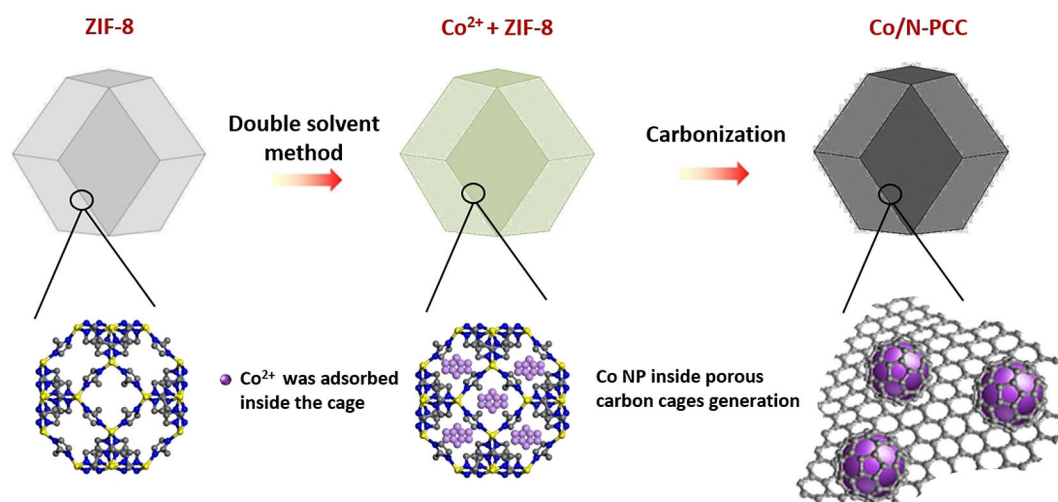
Figure 1. Synthesis of the Co/N-PCC electrocatalyst using ZIF-8 as the template through a two-step synthesis method including (1) the double-solvent immobilization and (2) calcination in Ar.

the best of our knowledge, it has not been used to synthesize bifunctional O_2 electrocatalysts. In the second step, Co ion immobilized ZIF-8 was calcined in Ar at high temperatures. We have previously optimized the calcination temperature of ZIF-8, and 900°C can efficiently carbonize ZIF-8 to yield N-doped and heterosporous carbon materials.[62] The imidazole rings in ZIF-8 contribute to the formation of graphite-like carbon framework, and high N contents in ZIF-8 (i.e., two N atoms per ligand, 2-methylimidazole) serve as N dopants for carbon framework. Co ions are expected to be reduced and nucleate into Co metal nanoparticles. A reference N–PCC electrocatalyst was also prepared using the similar synthesis procedure except that no Co precursors were added in the aqueous solvent.

2.2. Physicochemical Characterization of the Co/N-PCC Electrocatalyst

SEM and TEM first examined the morphology of as-synthesized electrocatalysts. As shown in Figure 2a, Co/N-PCC are polyhedral porous particles resembling the morphology of ZIF-8 particles. The corresponding EDS mappings in Figure 2b indicate the uniform distribution of C, N, O, and Co in Co/N–PCC. The TEM image in Figure 2c shows that spherical Co nanoparticles distribute uniformly in the porous carbon substrate. The average diameter of the Co nanoparticles is 6.2 nm. The high-resolution TEM image in Figure 2d shows that Co nanoparticles are wrapped by porous graphitized carbon shells (pink arrows in Figure 2d), which suggests that Co nanoparticles can promote the graphitization of carbon during the calcina-

tion.[63–64] Considering the size of ZIF-8 cavities is about 1.2 nm, TEM images in Figure 2 suggest that small Co nanoclusters formed in ZIF-8 cavities would diffuse out of carbonized ZIF-8 cages and nucleate into larger nanoparticles due to the Ostwald ripening effect.[65–66] Some hollow graphitized carbon cages are observed (red arrows in Figure 2d). The interconnected porous carbon cages are expected to provide efficient diffusion channels for reactants and intermediates in ORR and OER.[67] The intimate contact between Co nanoparticles and surrounding graphitized carbon cages may facilitate rapid electron transfers. Characteristic lattice spacings at 0.20, 0.18 and 0.12 nm are observed in the electron diffraction pattern of Co/N-PCC (Figure 2e), which correspond to the in-plane lattice spacings of Co metal (JCPDS File 15-0806) at 0.2047 nm (111), 0.1772 nm (200), and 0.1253 nm (220), respectively. This indicates the formation of metallic Co nanoparticles. Furthermore, the XRD pattern of Co/N-PCC (Figure 2f) also shows the diffraction peaks between 40° and 80°, which are aligned with to the typical (111), (200), and (220) reflections of Co-crystals (PDF No. 15-0806). In comparison, the broadened diffraction peak at around 25° can be assigned to carbon substrates, which is more clearly observed on the XRD pattern of N–PCC.

The porosity of electrocatalysts was further characterized by nitrogen sorption. Figure 3a shows that Co/N–PCC has the specific surface area of 434.5 $m^2 g^{-1}$, which is about half of that of N–PCC at 803.7 $m^2 g^{-1}$. The hysteresis loops observed in both samples indicate the existence of mesopores, which may originate from voids between carbon cages or the formation of porous carbon cages. Correspondingly, the pore size distributions in Figure 3b show both micropores and mesopores. The
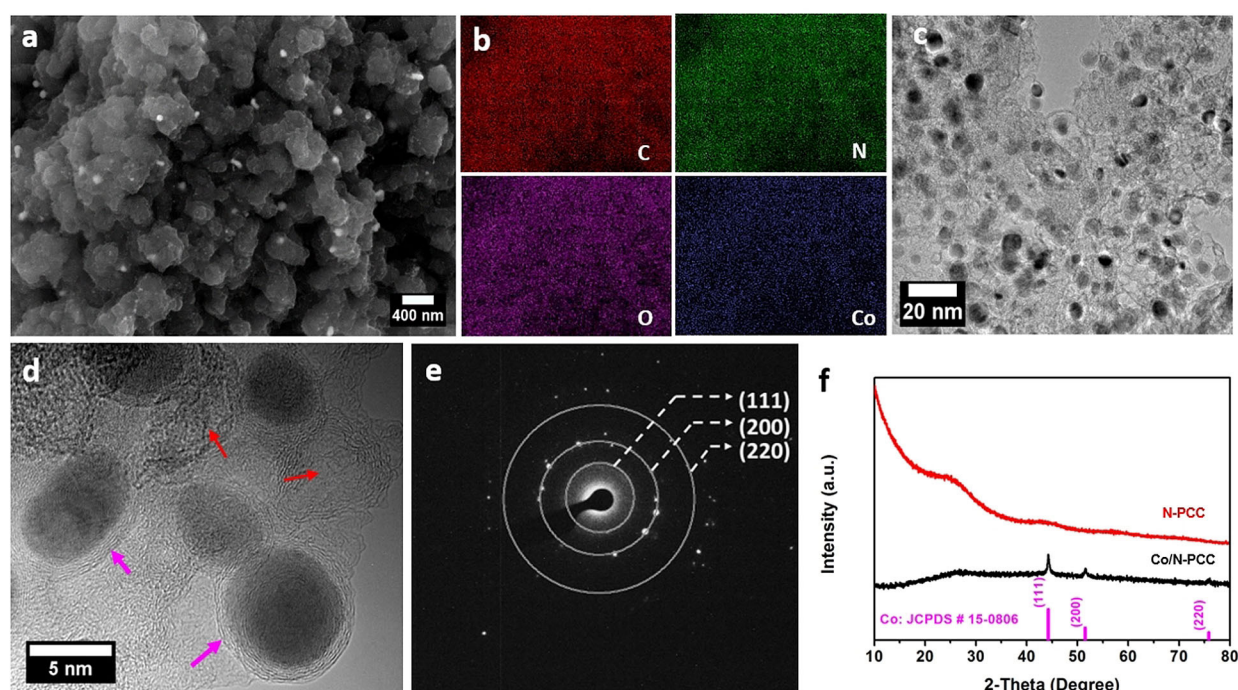

Figure 2. Morphology and crystallinity of Co/N–PCC electrocatalysts: a) SEM image of Co/N–PCC, b) the corresponding EDS mappings (C, N, O, and Co) from (a), c) TEM image of Co/N–PCC, d) a high resolution TEM image of Co nanoparticles in Co/N–PCC, e) the corresponding electron diffraction pattern from (d), and f) XRD patterns of Co/N–PCC and N–PCC, and standard crystal indices of Co metal (JCPDS number for Co: 15-0806) are shown at the bottom of (f).
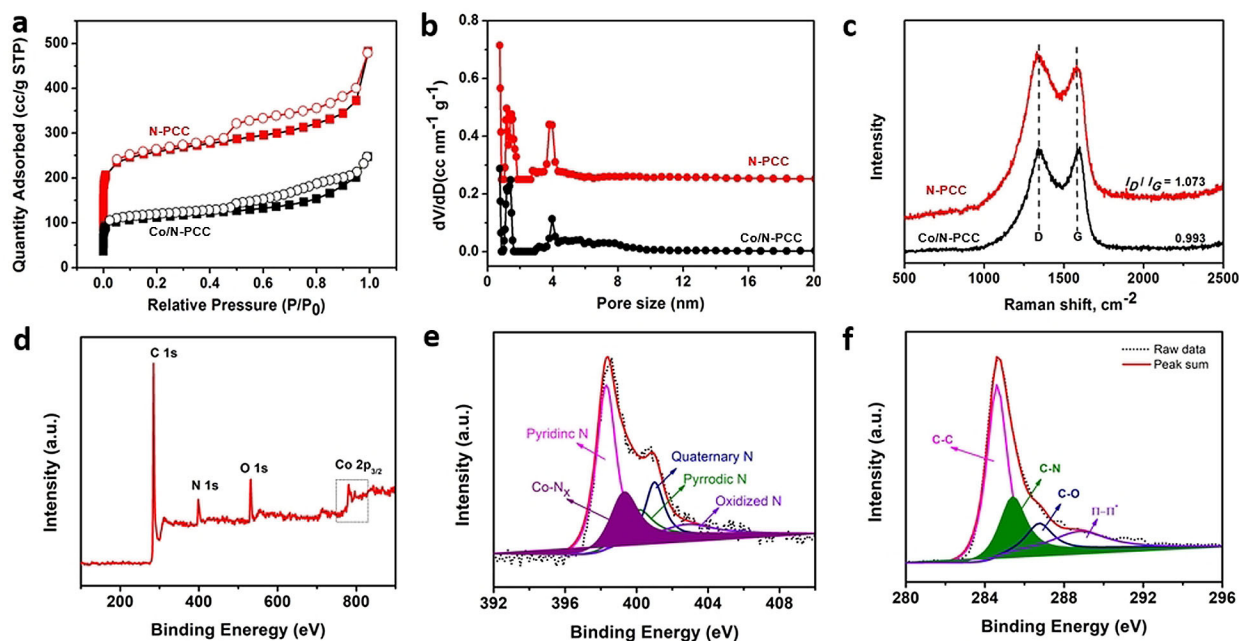
Figure 3. Physicochemical property characterization of Co/N–PCC and N–PCC. a) N_2 physisorption isotherms, b) pore size distribution, c) Raman spectra, d) XPS spectrum of Co/N–PCC, and the corresponding high-resolution XPS spectra of e) N 1s and f) C 1s.

micro-porosity in carbon materials is likely inherited from the microporous ZIF-8 template. And some micropores would be sacrificed during the graphitization of carbon, especially when Co nanoparticles catalyzed it. Meanwhile, some mesopores are generated when Co nanoparticles diffuse out of carbon cages. Raman spectra in Figure 3c show characteristic D-band and G-band peaks at 1335 and 1590 cm^{-1}, respectively. The D band peaks are originated from the disordered carbon, and the G band peaks are associated with the graphic carbon, respectively.[21] The intensity ratio of between the D and G band peaks (I_D/I_G) of Co/N-PCC at 0.993 is smaller than that of N-PCC at 1.073, indicating that Co nanoparticles assist the graphitization of carbon materials.

XPS was used to investigate the surface chemical properties of Co/N-PCC. The XPS spectrum in Figure 3d indicates the existence of C, O, N, and Co. The elemental analysis done by XPS indicates that Co/N-PCC contains a high N content of 11.09 at.%. As shown in Figure 3e, the high-resolution N1 s spectrum can be deconvoluted into five peaks, corresponding to pyridinic (398.4 eV), pyrrolic (400.1 eV), graphitic (401.2 eV), oxidized (403.2 eV) Ni species and Co-N$_x$ (399.3 eV), respectively. The pyridinic N is the dominant N species (29.3%), and there is also a significant fraction of N (15.4%) species coordinated with Co. Moreover, the high resolution of C1s spectrum in Figure 3f shows a C–N peak at 285.4 eV, indicating the doping of N in carbon materials. Overall, various physiochemical characterization results above confirm the formation of highly dispersed Co nanoparticles confined in nitrogen-doped porous carbon cages.

2.3. Oxygen Reduction and Oxygen Evolution Performance of Co/N–PCC

We first examined the catalytic performance of Co/N–PCC for ORR using electrocatalysts deposited on RDEs in the three-electron configuration, as described in the experimental section. Figure 4a shows the CV curves of Co/N–PCC and N–PCC at the scan rate of 100.0 mV s^{-1} in O_2-saturated 0.10 M KOH electrolyte. Distinct cathodic peaks are observed for both electrocatalysts, indicating their activity for ORR. The current density at the peak of Co/N–PCC is significantly higher than that of N–PCC, suggesting higher activity. Further, the peak potential of Co/N–PCC is more positive (90 mV) than that of N–PCC. LSV curves in Figure 4b show that Co/N–PCC has the limiting current density of 5.12 mA cm^{-2}, comparable to that of 20 wt.% Pt/C at 5.07 mA cm^{-2}, and much higher than that of N–PCC at 4.37 mA cm^{-2}. It should be noted that the ORR limiting current density can be affected by several experimental parameters, such as the flowing rate of purging oxygen gas in the electrolyte, the rotating speed of RDE, and the mass loading of electrocatalysts. The result reported here is comparable to those in several previous studies.[23,68–69] The half-wave potential (i.e., the potential at which the current is half of the limiting current) of Co/N–PCC is 0.838 mV, which is more positive than that of N–PCC at 0.771 mV, indicating a much higher activity for ORR with the presence of Co species. Moreover, the Tafel slopes determined from Figure 4c are 85, 176, and 75 mV dec^{-1} for Co/N–PCC, N–PCC, and Pt/C, respectively, suggesting that the ORR kinetics is faster on Co/N–PCC than on N–PCC, and is also comparable to Pt/C. The electron transfer number of ORR was determined by K-L plots shown in Figure 4d–e, indicating that the ORR on Co/N–PCC follows the efficient 4-electron pathway.
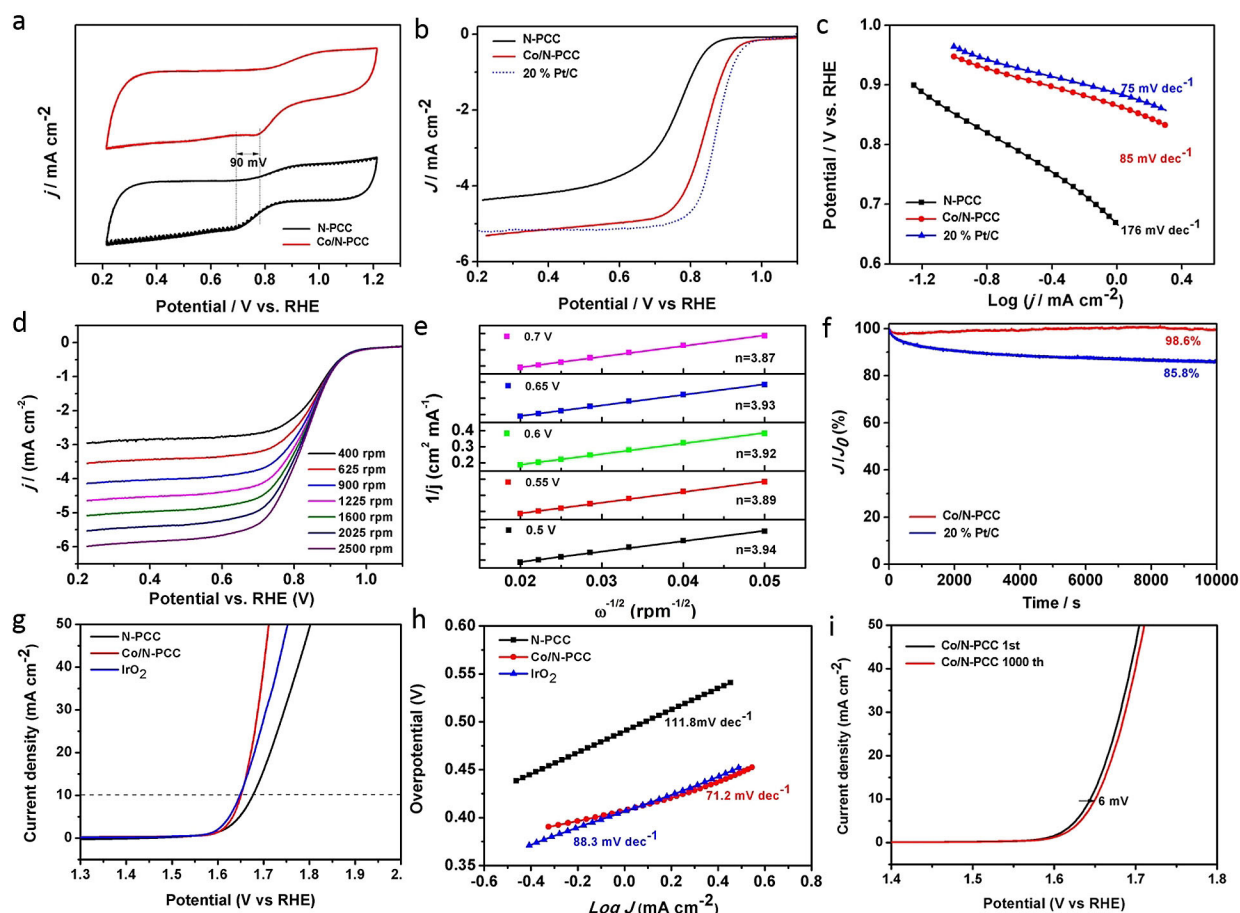
Figure 4. Catalytic performance of electrocatalysts for ORR and OER. a) CV curves of Co/N–PCC and N–PCC at the scan rate of 100.0 mV s^{-1}, b) the disk current density of Co/N–PCC, N–PCC and Pt/C from RDE voltammogram at the scan rate of 5 mV s^{-1} and the rotation rate of 1600 rpm. c) the corresponding ORR Tafel plots from (b), d) RDE voltammogram of Co/N–PCC at different RDE rotation rates from 400 to 2500 rpm, e) the corresponding K–L plots at the potentials from 0.5 to 0.7 V, f) durability of Co/N–PCC and Pt/C at 0.3 V vs. RHE for continuous ORR of 10000 s, g) OER LSV polarization curves of Co/N–PCC, N-PCC and IrO$_2$, h) the corresponding Tafel plots derived from (g), and (i) long-term stability test: LSV curves of Co/N–PCC at initial and after 1000th CV scanning.

These results clearly show that Co nanoparticles embedded in porous carbon cages have a significantly higher activity for ORR compared to carbon materials alone. The improved activity may be attributed to catalytically active sites on Co nanoparticles, as well as active sites related to Co–N$_x$.[70–71] We also carried out the chronoamperometric durability tests on Co/N–PCC and Pt/C at 0.30 V vs. RHE for 10000 s in the O$_2$-saturated 0.1 M KOH electrolyte. Figure 4f shows that Co/N–PCC can retain 98.6 % of its initial current density, which is higher than that of Pt/C (85.8 %), indicating its good durability. This may be attributed to the fact that porous crystalline carbon shells would protect Co nanoparticles.

Next, we evaluated the OER activity of electrocatalysts deposited on GCEs in 0.1 M KOH electrolyte. LSV polarization curves recorded at the scan rate of 5 mV s^{-1} are shown in Figure 4g. Co/N–PCC requires an overpotential (η_{10}) of 411 mV to reach the current density of 10 mA cm^{-2}, which is comparable to 418 mV required by IrO$_2$ and lower than 447 mV required by N–PCC, respectively. The corresponding Tafel slope of Co/N–PCC in Figure 4h is 71.2 mV dec^{-1}, which is smaller than that of N–PCC and IrO$_2$ at 111.8 and 88.3 mV dec^{-1}, respectively. The lower η_{10} and smaller Tafel slope of Co/N–PCC indicate its higher catalytic activity. Furthermore, the stability of Co/N–PCC is assessed by repeated

potential cycling for 1000 cycles, as shown in Figure 4i. Only a slight decay of the activity (6 mV) was observed based on the polarization curves after the long-term test, suggesting good durability of Co/N–PCC for OER.

2.4. Performance of Assembled Zn-Air Batteries

Since Co/N–PCC demonstrates good catalytic activities for both ORR and OER, we used it as a bifunctional O$_2$ electrocatalyst to assemble rechargeable Zn-air batteries. Figure 5a shows a schematic illustration of the assembled two-electrode Zn-air battery. A Zn foil was used as the anode, and the catalyst-loaded carbon cloth as air-cathode, with a catalyst loading of $\approx$ 1 mg cm^{-2}. 0.20 M ZnCl$_2$ was added into the 6.0 M KOH aqueous electrolyte to ensure the reversible anode reactions and rechargeable operation. Commercial Pt/C and IrO$_2$ electrocatalysts were also physically mixed (denoted as Pt/C + IrO$_2$) to assemble Zn-air batteries. As shown in Figure 5b, both types of batteries have similar open circuit voltages at around 1.48 V. The Co/N-PCC battery demonstrates the ideal charging and discharging curves, especially at higher current densities. Further, the Co/N-PCC battery delivered a power density of
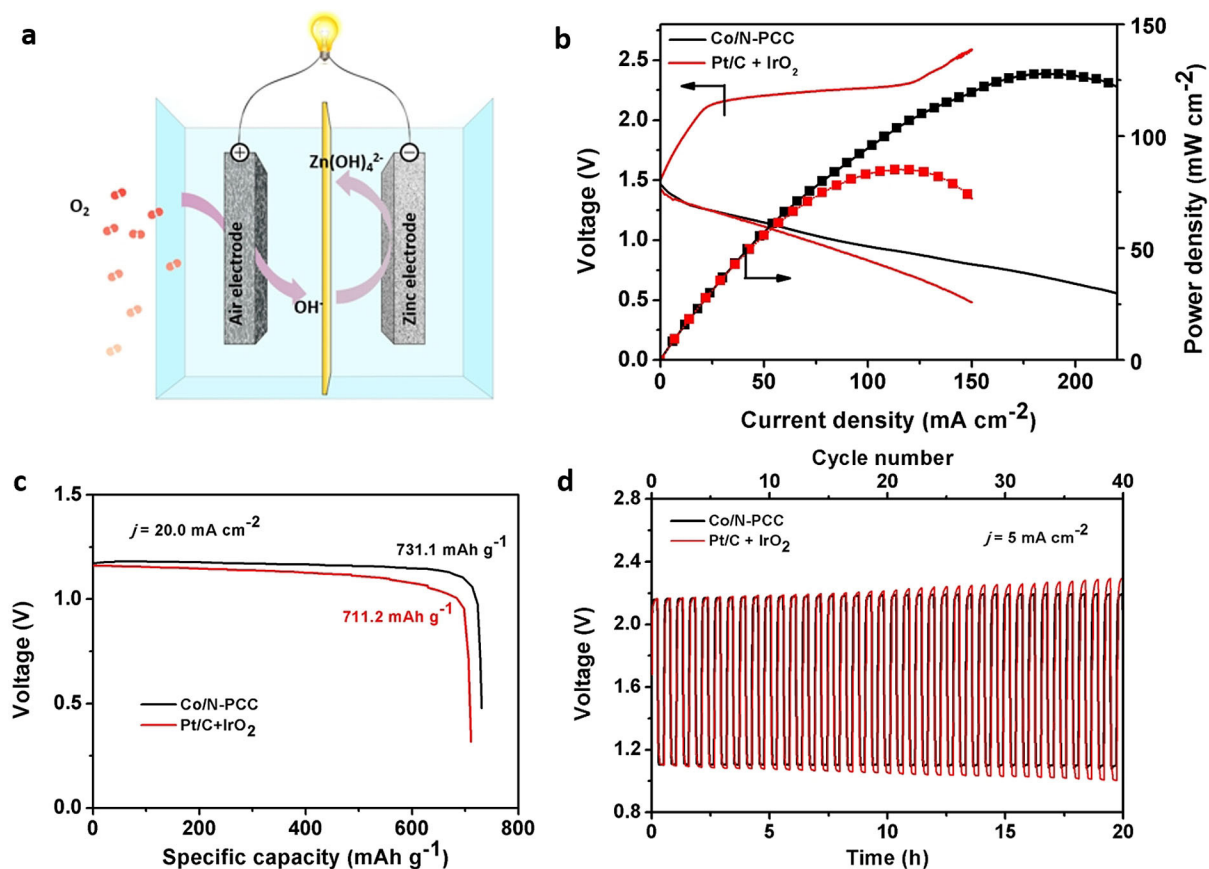
Figure 5. a) Schematic illustration of a two-electrode Zn-air battery. b) Charge and discharge polarization curves of the assembled Zn-air batteries using Co/N–PCC or Pt/C + IrO$_2$ as the O$_2$ electrocatalyst in air electrodes. c) Discharge curves of the Zn-air batteries at the discharging current density of 20.0 mA cm^{-2}. d) Charge/discharge cycling curves of the Zn-air batteries at the current density of 5.0 mA cm^{-2}.

127.86 mW cm^{-2}, which is higher than that provided by the Pt/C + IrO$_2$ battery at 85.07 mW cm^{-2}. It should be noted that the total catalyst loading is 1 mg cm^{-2}. Thus, only 0.5 mg cm^{-2} Pt/C works for ORR during discharging and 0.5 mg cm^{-2} IrO$_2$ works for OER during charging. Further, some active catalytic sites may not be exposed in the physical mixture Pt/C and IrO$_2$. Therefore, even though Pt/C has better ORR performance than Co/N-PCC and IrO$_2$ has similar OER performance as Co/N-PCC, the assembled Zn-air battery shows the inferior performance. Figure 5c shows that when the Co/N-PCC battery is discharged at the current density of 20.0 mA cm^{-2}, it delivers a stable discharge voltage around 1.12 V without obvious degradation in contrast to the Pt/C + IrO$_2$ battery. The specific capacity of the Co/N–PCC battery at 20.0 mA cm^{-2} is 731 mAh g^{-1} normalized to the mass of consumed Zn (89.1% of the theoretical capacity 820 mAh g^{-1}), and corresponds to a high energy density of 818.7 Wh kg^{-1} based on Zn (75.4% of the theoretical energy density 1086 Wh kg^{-1}). These performance data for Zn-air batteries are among one of the best results recently reported in the literature (see Table S3 in SI for a detailed comparison). We further tested the rechargeability and cycling durability of the batteries. As shown in Figure 5d, when cycled at a constant current density of 5.0 mA cm^{-2}, the Co/N–PCC battery delivers an initial discharge potential of 1.11 V and a charge potential of 2.16 V with a voltage gap of 1.07 V. After 40

charge/discharge cycles over 20 hours, the charge/discharge voltage gap only decreases by 40 mV, revealing excellent cycling stability and rechargeability. In contrast, the Pt/C + IrO$_2$ battery suffers significant activity decays during the charge/discharge cycling.

3. Conclusions

A high-performance bifunctional electrocatalyst for ORR and OER was prepared by confining Co nanoparticles in N doped porous carbon cages derived from ZIF-8. Co precursors were first impregnated into nanocages of ZIF-8 via capillary forces using the double solvent method. The optimized carbonization at 900 °C yields highly dispersed Co nanoparticles (with the average diameter of 6.2 nm) confined in N (11.4 at.%) doped porous carbon cages (434.5 m^2 g^{-1}). The electrocatalyst exhibits excellent ORR activity in 0.1 M KOH electrolyte with the half-wave potential of 0.838 V vs. RHE and has the electron transfer number of 3.9. Further, it also shows excellent OER activity in 0.1 M KOH electrolyte with the overpotential of 0.411 V at 10 mA cm^{-2} and a Tafel slope of 71.2 mV dec^{-1}. These outstanding performances are associated with the unique structural features of Co/N–PCC, including highly dispersed Co nanoparticles, N doped carbon materials, the formation of

Co–N$_x$ bonding as active catalytic sites, a large specific surface area and hierarchical pores. Besides, it also demonstrates excellent long-term catalytic activity stability, which may be attributed to the protection of Co nanoparticles in crystalline carbon shells. The electrocatalyst was used to fabricate air electrodes for rechargeable Zn-air batteries, demonstrating the open-circuit potential of 1.48 V, the specific capacity of 731.1 mAh g^{-1} (corresponding to the energy density of 818.7 Wh kgZn^{-1}), and excellent rechargeability with charging/discharging 40 cycles and the small decrease in the voltage gap by 40 mV. This work demonstrates a simple and efficient method to obtain stable metal nanoparticles confined in carbon cages for potential energy conversion applications.

Acknowledgments

Conflict of Interest

The authors declare no conflict of interest.

[1] F. Jaouen, E. Proietti, M. Lefevre, R. Chenitz, J. P. Dodelet, G. Wu, H. T. Chung, C. M. Johnston, P. Zelenay, *Energy Environ. Sci.* **2011**, *4*, 114–130.
[2] L. M. Dai, D. W. Chang, J. B. Baek, W. Lu, *Small* **2012**, *8*, 1130–1166.
[3] S. Zhai, H. E. Karahan, L. Wei, X. Chen, Z. Zhou, X. Wang, Y. Chen, *Energy Storage Mater.* **2017**, *9*, 221–228.
[4] F. Y. Cheng, J. Chen, *Chem. Soc. Rev.* **2012**, *41*, 2172–2192.
[5] R. Cao, J. S. Lee, M. L. Liu, J. Cho, *Adv. Energy Mater.* **2012**, *2*, 816–829.
[6] Z. L. Wang, D. Xu, J. J. Xu, X. B. Zhang, *Chem. Soc. Rev.* **2014**, *43*, 7746–7786.
[7] C. Galeano, C. Baldizzone, H. Bongard, B. Spliethoff, C. Weidenthaler, J. C. Meier, K. J. J. Mayrhofer, F. Schuth, *Adv. Funct. Mater.* **2014**, *24*, 220–232.
[8] J. Fu, Z. P. Cano, M. G. Park, A. Yu, M. Fowler, Z. Chen, *Adv. Mater.* **2017**, *29*, 1604685.
[9] X. Cai, L. Lai, J. Lin, Z. Shen, *Mater. Horiz.* **2017**, *4*, 945–976.
[10] J. Pan, Y. Y. Xu, H. Yang, Z. Dong, H. Liu, B. Y. Xia, *Adv. Sci.* **2018**, *5*, 1700691.
[11] Z. Ma, P. Pei, K. Wang, X. Wang, H. Xu, Y. Liu, G. peng, *J. Power Sources* **2015**, *274*, 56–64.
[12] X. Chen, Z. Zhou, H. E. Karahan, Q. Shao, L. Wei, Y. Chen, *Small* **2018**, *14*, 1801929.
[13] Y. Huang, Y. Wang, C. Tang, J. Wang, Q. Zhang, Y. Wang, J. Zhang, *Adv. Mater.* **2018**,1803800.
[14] J. Z. Ma, Z. H. Xiang, J. T. Zhang, *Sci. China Chem.* **2018**, *61*, 592–597.
[15] L. Wang, Y. Wang, M. Wu, Z. Wei, C. Cui, M. Mao, J. Zhang, X. Han, Q. Liu, J. Ma, *Small* **2018**, *14*, 1800737.
[16] M. Wu, Y. Wang, Z. Wei, L. Wang, M. Zhuo, J. Zhang, X. Han, J. Ma, *J. Mater. Chem. A* **2018**, *6*, 10918–10925.
[17] W. Gan, D. Zhou, L. Zhou, Z. Zhang, J. Zhao, *Electrochim. Acta* **2015**, *182*, 430–436.
[18] B. Hwang, E.-S. Oh, K. Kim, *Electrochim. Acta* **2016**, *216*, 484–489.
[19] G. L. Tian, Q. Zhang, B. S. Zhang, Y. G. Jin, J. Q. Huang, D. S. Su, F. Wei, *Adv. Funct. Mater.* **2014**, *24*, 5956–5961.
[20] Z. Y. Wu, X. X. Xu, B. C. Hu, H. W. Liang, Y. Lin, L. F. Chen, S. H. Yu, *Angew. Chem. Int. Ed.* **2015**, *54*, 8179–8183; *Angew. Chem.* **2015**, *127*, 8297–8301.
[21] X. C. Chen, L. Wei, Y. Q. Wang, S. L. Zhai, Z. B. Chen, S. W. Tan, Z. Zhou, A. K. Ng, X. Z. Liao, Y. Chen, *Energy Storage Mater.* **2018**, *11*, 134–143.
[22] M. X. Shen, C. T. Wei, K. L. Ai, L. H. Lu, *Nano Res.* **2017**, *10*, 1449–1470.
[23] L. Wei, H. E. Karahan, S. L. Zhai, H. W. Liu, X. C. Chen, Z. Zhou, Y. J. Lei, Z. W. Liu, Y. Chen, *Adv. Mater.* **2017**, *29*, 1701410.
[24] N. T. Suen, S. F. Hung, Q. Quan, N. Zhang, Y. J. Xu, H. M. Chen, *Chem. Soc. Rev.* **2017**, *46*, 337–365.
[25] L. Köhler, L. Szabadics, C. Jooss, M. Risch, *Batteries & Supercaps* **2018**, doi:10.1002/batt.201800119.
[26] H. Osgood, S. V. Devaguptapu, H. Xu, J. Cho, G. Wu, *Nano Today* **2016**, *11*, 601–625.
[27] G. Q. Zhang, B. Y. Xia, C. Xiao, L. Yu, X. Wang, Y. Xie, X. W. Lou, *Angew. Chem. Int. Ed.* **2013**, *52*, 8643–8647; *Angew. Chem.* **2013**, *125*, 8805–8809.
[28] J. Pan, X. L. Tian, S. Zaman, Z. Dong, H. Liu, H. S. Park, B. Y. Xia, *Batteries & Supercaps* **2018**, doi:10.1002/batt.201800082.
[29] M. H. Yu, Z. K. Wang, C. Hou, Z. L. Wang, C. L. Liang, C. Y. Zhao, Y. X. Tong, X. H. Lu, S. H. Yang, *Adv. Mater.* **2017**, *29*, 1602868.
[30] X. Liu, L. M. Dai, *Nat. Rev. Mater.* **2016**, *1*, 1–12.
[31] S. Chen, S. Chen, J. Zhang, *Batteries & Supercaps* **2018**, doi:10.1002/batt.201800105.
[32] S. Chen, S. Chen, J. Zhang, *Batteries & Supercaps* **2019**, *0*, doi:10.1002/batt.201800105.
[33] Y. J. Wang, D. P. Wilkinson, J. J. Zhang, *Chem. Rev.* **2011**, *111*, 7625–7651.
[34] C. Galeano, J. C. Meier, M. Soorholtz, H. Bongard, C. Baldizzone, K. J. J. Mayrhofer, F. Schuth, *ACS Catal.* **2014**, *4*, 3856–3868.
[35] S. Ikeda, S. Ishino, T. Harada, N. Okamoto, T. Sakata, H. Mori, S. Kuwabata, T. Torimoto, M. Matsumura, *Angew. Chem. Int. Ed.* **2006**, *45*, 7063–7066; *Angew. Chem.* **2006**, *118*, 7221–7224.
[36] R. Liu, S. M. Mahurin, C. Li, R. R. Unocic, J. C. Idrobo, H. J. Gao, S. J. Pennycook, S. Dai, *Angew. Chem. Int. Ed.* **2011**, *50*, 6799–6802; *Angew. Chem.* **2011**, *123*, 6931–6934.
[37] S. Chen, J. Bi, Y. Zhao, L. Yang, C. Zhang, Y. Ma, Q. Wu, X. Wang, Z. Hu, *Adv. Mater.* **2012**, *24*, 5593–5599.
[38] J. P. Han, G. Y. Xu, B. Ding, J. Pan, H. Dou, D. R. MacFarlane, *J. Mater. Chem. A* **2014**, *2*, 5352–5357.
[39] S. H. Liu, J. Li, X. Yan, Q. F. Su, Y. H. Lu, J. S. Qiu, Z. Y. Wang, X. D. Lin, J. L. Huang, R. L. Liu, B. N. Zheng, L. Y. Chen, R. W. Fu, D. C. Wu, *Adv. Mater.* **2018**, *30*, 1706895.
[40] S. W. Tan, X. C. Chen, S. L. Zhai, A. Ebrahimi, T. Langrish, Y. Chen, *Energy* **2018**, *147*, 308–316.
[41] S. K. Park, H. Lee, M. S. Choi, D. H. Suh, P. Nakhanivej, H. S. Park, *Energy Storage Mater.* **2018**, *12*, 331–340.
[42] M. G. Wu, Y. Q. Wang, Z. X. Wei, L. Wang, M. Zhuo, J. T. Zhang, X. P. Han, J. M. Ma, *J. Mater. Chem. A* **2018**, *6*, 10918–10925.
[43] Y. Zhang, T. T. Qu, K. Xiang, Y. Shen, S. Y. Chen, M. J. Xie, X. F. Guo, *J. Mater. Chem. A* **2018**, *6*, 2353–2359.
[44] M. Y. Liu, J. Niu, Z. P. Zhang, M. L. Dou, F. Wang, *Nano Energy* **2018**, *51*, 366–372.
[45] G. L. Wang, X. P. Chen, Z. L. Cui, S. C. Yue, F. S. Zhang, *Agric. Ecosystems & Environ.* **2014**, *197*, 293–300; *Environ.* **2014**, 197, 293–300.
[46] A. Aijaz, A. Karkamkar, Y. J. Choi, N. Tsumori, E. Ronnebro, T. Autrey, H. Shioyama, Q. Xu, *J. Am. Chem. Soc.* **2012**, *134*, 13926–13929.
[47] L. Zhu, D. Z. Zheng, Z. F. Wang, X. S. Zheng, P. P. Fang, J. F. Zhu, M. H. Yu, Y. X. Tong, X. H. Lu, *Adv. Mater.* **2018**, *30*, 1805268.
[48] W. Xia, J. H. Zhu, W. H. Guo, L. An, D. G. Xia, R. Q. Zou, *J. Mater. Chem. A* **2014**, *2*, 11606–11613.
[49] B. H. Chen, X. B. He, F. X. Yin, H. Wang, D. J. Liu, R. X. Shi, J. N. Chen, H. W. Yin, *Adv. Funct. Mater.* **2017**, *27*, 1700795.
[50] Y. Jiang, Y. P. Deng, J. Fu, D. U. Lee, R. L. Liang, Z. P. Cano, Y. S. Liu, Z. Y. Bai, S. Hwang, L. Yang, D. Su, W. G. Chu, Z. W. Chen, *Adv. Energy Mater.* **2018**, *8*, 1702900.
[51] P. Q. Yin, T. Yao, Y. Wu, L. R. Zheng, Y. Lin, W. Liu, H. X. Ju, J. F. Zhu, X. Hong, Z. X. Deng, G. Zhou, S. Q. Wei, Y. D. Li, *Angew. Chem. Int. Ed.* **2016**, *55*, 10800–10805; *Angew. Chem.* **2016**, *128*, 10958–10963.
[52] D. Esken, S. Turner, O. I. Lebedev, G. Van Tendeloo, R. A. Fischer, *Chem. Mater.* **2010**, *22*, 6393–6401.
[53] H. L. Jiang, B. Liu, T. Akita, M. Haruta, H. Sakurai, Q. Xu, *J. Am. Chem. Soc.* **2009**, *131*, 11302–11303.

[54] H. L. Jiang, T. Akita, T. Ishida, M. Haruta, Q. Xu, *J. Am. Chem. Soc.* **2011**, *133*, 1304–1306.

[55] C. Wang, K. E. deKrafft, W. B. Lin, *J. Am. Chem. Soc.* **2012**, *134*, 7211–7214.

[56] Q. H. Yang, Q. Xu, H. L. Jiang, *Chem. Soc. Rev.* **2017**, *46*, 4774–4808.

[57] Y. Z. Chen, Y. X. Zhou, H. W. Wang, J. L. Lu, T. Uchida, Q. Xu, S. H. Yu, H. L. Jiang, *ACS Catal.* **2015**, *5*, 2062–2069.

[58] M. Imperor-Clerc, D. Bazin, M. D. Appay, P. Beaunier, A. Davidson, *Chem. Mater.* **2004**, *16*, 1813–1821.

[59] X. C. Huang, Y. Y. Lin, J. P. Zhang, X. M. Chen, *Angew. Chem. Int. Ed.* **2006**, *45*, 1557–1559; *Angew. Chem.* **2006**, *118*, 1587–1589.

[60] K. S. Park, Z. Ni, A. P. Cote, J. Y. Choi, R. D. Huang, F. J. Uribe-Romo, H. K. Chae, M. O'Keeffe, O. M. Yaghi, *Proc. Natl. Acad. Sci. U S A* **2006**, *103*, 10186–10191.

[61] S. R. Venna, M. A. Carreon, *J. Am. Chem. Soc.* **2010**, *132*, 76–78.

[62] Y. Lei, L. Wei, S. Zhai, Y. Wang, H. E. Karahan, X. Chen, Z. Zhou, C. Wang, X. Sui, Y. Chen, *Mater. Chem. Front.* **2018**, *2*, 102–111.

[63] Y. M. Chen, L. Yu, X. W. Lou, *Angew. Chem. Int. Ed.* **2016**, *55*, 5990–5993; *Angew. Chem.* **2016**, *128*, 6094–6097.

[64] J. Meng, C. Niu, L. Xu, J. Li, X. Liu, X. Wang, Y. Wu, X. Xu, W. Chen, Q. Li, Z. Zhu, D. Zhao, L. Mai, *J. Am. Chem. Soc.* **2017**, *139*, 8212–8221.

[65] T. W. Hansen, A. T. Delariva, S. R. Challa, A. K. Datye, *Acc. Chem. Res.* **2013**, *46*, 1720–1730.

[66] X. W. Lou, C. L. Yuan, E. Rhoades, Q. Zhang, L. A. Archer, *Adv. Funct. Mater.* **2006**, *16*, 1679–1684.

[67] J. Tang, R. R. Salunkhe, H. B. Zhang, V. Malgras, T. Ahamad, S. M. Alshehri, N. Kobayashi, S. Tominaka, Y. Ide, J. H. Kim, Y. Yamauchi, *Sci. Rep.* **2016**, *6*, 30295–30302.

[68] C. Tang, B. Wang, H. F. Wang, Q. Zhang, *Adv. Mater.* **2017**, *29*, 1703185.

[69] Y. Y. Liang, Y. G. Li, H. L. Wang, J. G. Zhou, J. Wang, T. Regier, H. J. Dai, *Nat. Mater.* **2011**, *10*, 780–786.

[70] K. Strickland, E. Miner, Q. Jia, U. Tylus, N. Ramaswamy, W. Liang, M. T. Sougrati, F. Jaouen, S. Mukerjee, *Nat. Commun.* **2015**, *6*, 7343–7350.

[71] R. Zhou, S. Z. Qiao, *Chem. Commun.* **2015**, *51*, 7516–7519.